JGR Space Physics

RESEARCH ARTICLE
10.1029/2024JA032485

Atmospheric and Ionospheric Responses to Orographic Gravity Waves Prior to the December 2022 Cold Air Outbreak

P. A. Inchin[1,2], A. Bhatt[3], M. Bramberger[4], S. Chakraborty[5], S. Debchoudhury[2], and C. Heale[2]

[1]Computational Physics, Inc., Springfield, VA, USA, [2]Center for Space and Atmospheric Research, Embry-Riddle Aeronautical University, Daytona Beach, FL, USA, [3]SRI International, Menlo Park, CA, USA, [4]NorthWest Research Associates, Boulder Office, Boulder, CO, USA, [5]Center for Space Science and Engineering Research, Virginia Tech, Blacksburg, VA, USA

Key Points:

- Alaskan ridge circulation led to southward shifting of polar jetstream and the generation of large-amplitude orographic gravity waves (GWs) over Rocky Mountains
- The breaking of upward propagating GWs resulted in ionospheric disturbances from secondary waves across the entire Continental United States for several days
- Super Dual Auroral Radar Network observations are suitable for the detection of small-scale and amplitude traveling ionospheric disturbances induced by atmospheric waves

Correspondence to:
P. A. Inchin,
pinchin@cpi.com

Citation:
Inchin, P. A., Bhatt, A., Bramberger, M., Chakraborty, S., Debchoudhury, S., & Heale, C. (2024). Atmospheric and ionospheric responses to orographic gravity waves prior to the December 2022 cold air outbreak. *Journal of Geophysical Research: Space Physics*, *129*, e2024JA032485. https://doi.org/10.1029/2024JA032485

Received 15 FEB 2024
Accepted 22 MAY 2024

Author Contributions:
Conceptualization: P. A. Inchin, S. Chakraborty, S. Debchoudhury, C. Heale
Data curation: P. A. Inchin, S. Chakraborty, S. Debchoudhury, C. Heale
Formal analysis: P. A. Inchin, A. Bhatt, M. Bramberger, S. Chakraborty, S. Debchoudhury, C. Heale
Funding acquisition: S. Debchoudhury
Investigation: P. A. Inchin, M. Bramberger, S. Chakraborty, S. Debchoudhury, C. Heale
Methodology: P. A. Inchin, A. Bhatt, M. Bramberger, S. Chakraborty, S. Debchoudhury, C. Heale
Project administration: S. Debchoudhury
Resources: P. A. Inchin, S. Debchoudhury, C. Heale
Software: P. A. Inchin, S. Chakraborty, S. Debchoudhury, C. Heale

Abstract Mountain waves are known sources of fluctuations in the upper atmosphere. However, their effects over the Continental United States (CONUS) are considered modest as compared to hot spots such as the Southern Andes. Here, we present an observation-guided case study examining the dynamics of gravity waves (GWs) and their impacts on the ionosphere over the CONUS prior to the cold air outbreak in December 2022, which resulted from a significant distortion of the tropospheric polar vortex. The investigation relies on MERRA-2 and ERA5 reanalysis data sets for the climatological contextualization, analysis of GWs based on National Aeronautics and Space Administration Aqua satellite's Atmospheric Infrared Sounder, 557.7 and 630.0 nm airglow emission observations, and the measurements of ionospheric disturbances retrieved from Global Navigation Satellite System signal-based total electron content (TEC) and Super Dual Auroral Radar Network observations. We demonstrate that the tropospheric polar jet stream shifted toward the Rocky Mountains, generated large amplitude GWs (up to 11 K of brightness temperature), which, aided by winter-time winds over mid-latitudes, could propagate to mesospheric heights. The breaking of GWs plausibly led to the generation of a plethora of secondary acoustic and GWs that eventually emerged as the sources of extensive ionospheric fluctuations of ∼3–30 min periods and up to 0.7 TECu, observed across the entire CONUS for several days. This case offers a valuable demonstration of the interplay between tropospheric circulation and the ionosphere over CONUS, pointing to the need for a better understanding of wave-driven deep-atmosphere coupled dynamics.

Plain Language Summary Atmospheric waves generated by wind flows over the mountains (mountain waves, MWs) play an important role in the dynamics of the upper atmosphere and its ionized part, the ionosphere. The days preceding the December 2022 North American Winter Storm demonstrated unusually long-living fluctuations in the ionosphere across the whole Continental United States (CONUS). The study of this event, reported in this manuscript, incorporates the analysis of climatological data sets, remote and satellite observations of wave-related fluctuations in the stratosphere, mesosphere, and the ionosphere. We find that the variability of strong westward winds in the troposphere, flowing over northern part of CONUS (so-called polar jet stream), led to the generation of MWs over the Rocky Mountains. MWs, supported by the winter-time wind stratification in the northern hemisphere, likely propagated to altitudes up to ∼90 km and gave rise to secondary atmospheric waves, which in turn induced large amplitude fluctuations in the ionosphere at altitudes of ∼250–350 km observed in Global Navigation Satellite System total electron content and Super Dual Auroral Radar observations. This unique event serves as an important example of the interconnected dynamics between the lower and upper layers of the atmosphere over mid-latitude regions.

1. Introduction

Gravity waves (GWs) are important contributors to the circulation and temperature structure of the atmosphere resulting from their momentum and energy deposition over the course of their propagation (Fritts & Alexander, 2003). The sources of GWs are commonly categorized as orographic, that is, wind flow over topography (Eckermann & Preusse, 1999; McFarlane, 1987; Sandu et al., 2019; Smith, 2019), and non-orographic, resulting, for example, from convection and precipitation, jets, fronts, natural hazards, as well as the coupling with oceans (Hertzog et al., 2008; Holt et al., 2017; Inchin et al., 2020). While the former are considered to be significant

Supervision: P. A. Inchin, S. Debchoudhury
Validation: P. A. Inchin, A. Bhatt, M. Bramberger, S. Chakraborty, S. Debchoudhury, C. Heale
Visualization: P. A. Inchin, S. Chakraborty, S. Debchoudhury, C. Heale
Writing – original draft: P. A. Inchin, A. Bhatt, M. Bramberger, S. Chakraborty, S. Debchoudhury, C. Heale

sources of GWs, which may propagate horizontally (e.g., Ehard et al., 2017; Preusse et al., 2009; Sato et al., 2012), their dynamics are still mostly confined around mountainous regions, such as the Andes, Antarctic Peninsula, European Alps, New Zealand and Himalayas (Bossert et al., 2017; Heale et al., 2020; Hoffmann et al., 2013; Niranjan Kumar et al., 2012). In comparison, non-orographic GWs cover all regions, potentially producing comparable-to-orographic GW impacts on the atmosphere (Plougonven & Zhang, 2014).

The exponential decrease of mass density with altitude leads to the growth of GW amplitudes as they propagate upward (Hines, 1960). GW dissipation or nonlinear evolution, such as self-acceleration and breaking, can also result in the generation of secondary acoustic and GWs (hereafter, sAGWs), spanning periods from minutes to hours (e.g., Garcia & Solomon, 1985; Hickey & Cole, 1988; Lund & Fritts, 2012; Vadas & Becker, 2019). In the ionosphere, GWs and sAGWs induce plasma fluctuations, commonly called traveling ionospheric disturbances (TIDs), which are routinely detected with in-situ and remote sensing instruments (e.g., Liu et al., 2019; Regmi & Maharjan, 2015; Smith et al., 2002; Vadas et al., 2019). Although considered essential drivers of ionospheric dynamics and electrodynamic effects, locally and in magnetically conjugate regions (Chou et al., 2023; Zawdie et al., 2022), the impacts of GWs and sAGWs on the ionosphere are yet to be quantified. The understanding of these impacts is also important for robust high frequency (HF) communication, over-the-horizon radar operation and for the need of accurate predictions of ionospheric state for precise pointing positioning applications (Paziewski et al., 2022; Timoté et al., 2020). Likewise, these waves may also favor the seeding of plasma irregularities at low-latitude region, which, in turn, may results in the disruption of satellite navigation and communication (Huba & Liu, 2020; Klenzing et al., 2023).

Cold air outbreaks (CAO) are large-scale severe hazards occurring at mid-latitudes during winter time driven by the equatorward displacement of cold air from polar regions (e.g., Grotjahn et al., 2016; Konrad & Colucci, 1989; Millin et al., 2022). In the northern hemisphere, and particularly over the Continental United States (CONUS), CAOs bring widespread socio-economial difficulties, including environmental and infrastructure damage, transportation delays, and most importantly cold-related fatalities. One such CAO occurred at the end of December 2022, causing extreme winter storm conditions across the CONUS (https://www.weather.gov/mrx/December_2022_Record_Cold). It resulted in record-breaking cold temperatures across many states and is considered a historic arctic outbreak. Figure 1 illustrates the 2-m temperature (T2M) anomalies as derived from the fifth generation atmospheric reanalysis of the global climate by Medium-Range Weather Forecasts (ERA5, the details of data processing are provided Section 2), with a mean state derived for years 1988–2021 for each time epoch illustrated. The outbreak brought cold air from the polar regions starting from roughly the 21st of December, entering from the northwest and north of the Great Plains (Figures 1a and 1b). During the following days, the CAO spread across the central part of the CONUS and shifted toward the Mid-Atlantic United States, additionally bringing cold air to the South (Figures 1c and 1d). During the CAO, the temperature anomalies reached −34 K.

At the same time, the days before the December 2022 CAO expansion toward CONUS exhibited abnormal atmospheric and ionospheric dynamics, and it is these dynamics that form the topic of our report. This study, based on climatological model reanalyzes, National Aeronautics and Space Administration (NASA) Aqua satellite's Atmospheric Infrared Sounder (AIRS) and ground-based mesospheric and ionospheric airglow observations, as well as Global Navigation Satellite System (GNSS) total electron content (TEC) and SuperDARN data sets, illustrates a unique event of marked tropospheric wave activity impacts the ionosphere over CONUS. It shows that even comparatively moderate winds over the Rocky mountains may result in effective generation of orographic GWs, and their following substantial impact on the ionosphere through the breaking and generation of sAGWs detectable over the whole CONUS for several days.

The manuscript is structured as follows. Section 2 includes a description of the data sets used and the methodology for their processing. Section 3 presents the results and their interpretation, and Section 4 summarizes the outcomes of the study and scopes the opportunities and future needs for the investigation of ionospheric responses to low-altitude dynamics at mid-latitudes.

2. Data Sets and Processing Methodology

In order to understand the meteorological preconditions resulting in the generation of GWs over the northwest of the CONUS, we used fifth generation European Centre for Medium-Range Weather Forecasts reanalysis for the global climate and weather reanalysis data sets ERA5. For geopotential height analysis, horizontal, and vertical

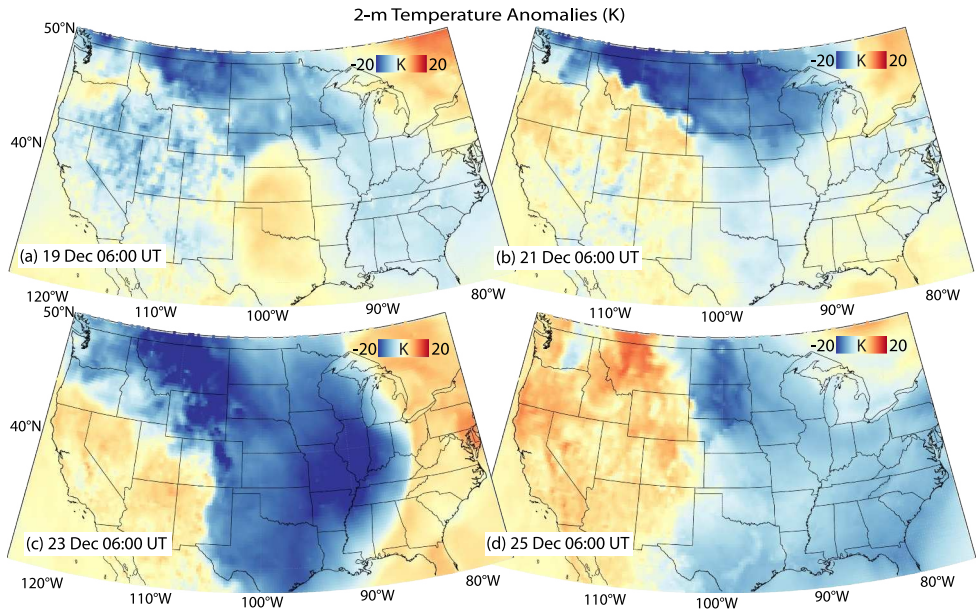

Figure 1. 2-m temperature (T2M) anomalies retrieved from ERA5 reanalysis data set for four time epochs in December 2022. The mean state is derived from the same data set from the years 1988–2021 and subtracted from T2M at each time epoch demonstrated.

velocity we used ERA5 hourly data on pressure levels from 1940 to present. This data product is provided at 0.25° and 1 hr spatial and temporal resolution, respectively, at 37 pressure levels from 1,000 hPa to 1 hPa. Geopotential height is derived by dividing the geopotential data product by the Earth's gravitational acceleration, g (9.80665 ms^{-2}). The mean state for geopotential height is calculated as an average value between 2001 and 2021 for each day. The mean state of T2M was derived using ERA5 hourly data on single levels between 1988 and 2021 and then subtracted from data of December 2022 to obtain T2M anomalies. Additionally, we used MERRA2 3-hourly, instantaneous assimilated meteorological fields V5.12.4 for the analysis of winds.

To investigate GW-driven fluctuations in the stratosphere, we utilized the 4.3 μm band brightness temperature (BT) observations from the AIRS instrument onboard NASA's Aqua satellite. The AIRS BT data has been processed using channels with a peak emission intensity at 35 km altitude (Hoffmann et al., 2013). To investigate GWs in the upper atmosphere and their impact on the ionosphere, we used green line 557.7 nm at ∼95 km altitude and red line 630.0 nm at ∼250 km altitude airglow emission observations from imagers operated by the Mid-latitude Allsky-imaging Network for GeoSpace Observations (MANGO) network (Bhatt et al., 2023). Among those operational during the event, we find the imagers installed at Christmas Valley Observatory (CVO, 43.2°N/120.7°W) and Capitol Reef Field Station (CFS, 38.18°N/111.18°W) to be the most convincing to demonstrate the dynamics of our interest. The spatial coverage of green and red line emission imagers (field-of-view, FOV) are ∼500 km and ∼1,800 km in diameter, with a respective temporal resolution of 4 and 8 min per image. To retrieve the fluctuations, we calculated a sequential differencing of the images, removing a mean value from each.

The investigation of TIDs over the CONUS was also based on collected and processed 1, 15, and 30 s sampling rate GNSS TEC observations. The processing of GNSS signal measurements and the derivation of vertical TEC (vTEC) were performed using authors' software and the details of the methodology are provided in Inchin et al. (2023). Signal phase and pseudorange observations with GPS, GLONASS and Galileo satellites are processed from ∼2,800 stations between 11th and 27th of December 2022. For consistency, an altitude of 300 km was used as an ionospheric shell height for the calculation of the ionospheric pierce point (IPP) locations. The filtering of vTEC yields the perturbation quantities, representative of prevailing TIDs. The usage of specific high- and band-pass Butterworth filters are further discussed in the Results section. The characteristics of the aforementioned observational systems are summarized in Table 1.

As an ancillary data set to characterize TIDs, we used the Super Dual Auroral Radar Network (SuperDARN) observations. SuperDARN is an international collaboration of high-frequency radars, operating between 8 and

Table 1
The Characteristics of Observational Systems

#	Observations	Sampling rate	Spatial resolution	Sensitivity/noise level
1.	AIRS 4.3 micron BT	N/A	14×14 km^2 at nadir, 1,780 km-wide scan	$\lambda_x \geq 30$ km, $\lambda_z \geq 10$–15 km
2.	557.7 nm emission	2 min	~1 km zenith/diam ~ 500 km FOV	≥5 min
3.	630.0 nm emission	4 min	~3.5 km zenith/diam ~ 1,800 km FOV	≥9 min
4.	GNSS TEC	1–30 s	~$0.12 \times 0.12°$	TIDs ≤ 2 hr/~0.02 TECu

18 MHz, distributed across the middle, high, and polar latitudes of both hemispheres (Chisham et al., 2007; Greenwald et al., 1985; Martin et al., 2024; Nishitani et al., 2019). One radar scan typically comprises 16–20 azimuth beam soundings beginning at a range of 180 km, with subsequent range gates spaced at 45 km for a total of 75–110 range gates. For the observations presented, the scans were performed using an integration time of 6 s with a resulting time cadence of 2 min for each beam cycling through all the range gates. The SuperDARN radars operated in a 6-s beam sounding mode, facilitating a complete radar sweep within a 2-min scan time. SuperDARN observations primarily consist of two types of backscatters, namely, ionospheric and ground scatter (GS). Ionospheric scatter is generated when a transmitted signal is reflected from ionospheric irregularities. In the case of GS, due to a high daytime vertical gradient in ionospheric refractive index, the rays bend toward the ground and are reflected from surface roughness, and return to the radar following the same paths. Previous studies used SuperDARN back-scattered return power of the GS observations to identify and characterize TIDs (e.g., Frissell et al., 2014). In this study, we use the back-scattered return power of the GS to investigate GW-generated TIDs over the CONUS.

3. Results

3.1. Climatological Context of the Event

We start with a discussion of the polar region climatology that preceded the December 2022 CAO. Figures 2a–2d illustrates snapshots of GPH anomalies at the 500 hPa level between the 17–25 of December. Large positive GPH anomalies up to ~500 m over and northwest of Alaska, as well as positive anomaly up to ~300 m south of Greenland and Hudson bay were present on 17th of December. The ridges started forming on the ~15 of December (see the animation in the Supplemental Materials, SM, https://datacommons.erau.edu/datasets/v7342nzsm3/1) with the simultaneous forming of a trough over the northwest of the CONUS. This pattern, the Alaskan ridge and the ridge over and around Greenland, resembles a well documented pattern, commonly called the Alaskan Ridge regime, that can precede CAOs over the CONUS (Cellitti et al., 2006; Lee et al., 2019; Millin et al., 2022). During the day of CAO onset (21st of December), a rise in GPH anomaly occurred over Hudson Bay, which stayed practically at the same position, while the ridge over Alaska shifted toward the Siberian Arctic. Meanwhile, the negative anomaly expanded over larger northern regions of the CONUS. GPH data set during two days after the CAO onset (22–23 of December) demonstrates further expansion of the Alaskan ridge, but shrinking of the ridge over Hudson Bay. At next days, both positive anomalies weakened in amplitude and had fully vanished by the 27th of December (see the animation). During 21–25 of December, the trough over the CONUS continued gradually shifting to the south and eastward, which favored the channeling of cold air from polar regions toward the CONUS.

The ridges at the 100 hPa level were comparable in their structure to the ones we find on the 500 hPa level, with GPH anomalies dominating over the Alaskan region and Greenland and a trough over Canada and the north of the CONUS (Figures 2e and 2f). The stratospheric polar vortex (SPV) also exhibited disturbances prior to, and during, the CAO but overall maintained its cold core (Figures 2g and 2h). The positive GPH anomaly shifted toward Siberia and the negative GPH anomaly expanded eastwards (Figure 2h). This combination of Arctic high and Alaskan Ridge patterns are commonly associated with CAOs (Kretschmer et al., 2018; Lee et al., 2019). The so-called split event of the SPV was earlier reported to be a result of a tropospheric blocking event (Martius et al., 2009), but the role of tropospheric activity on SPV for this event requires further investigations through modeling case studies (Birner & Albers, 2017).

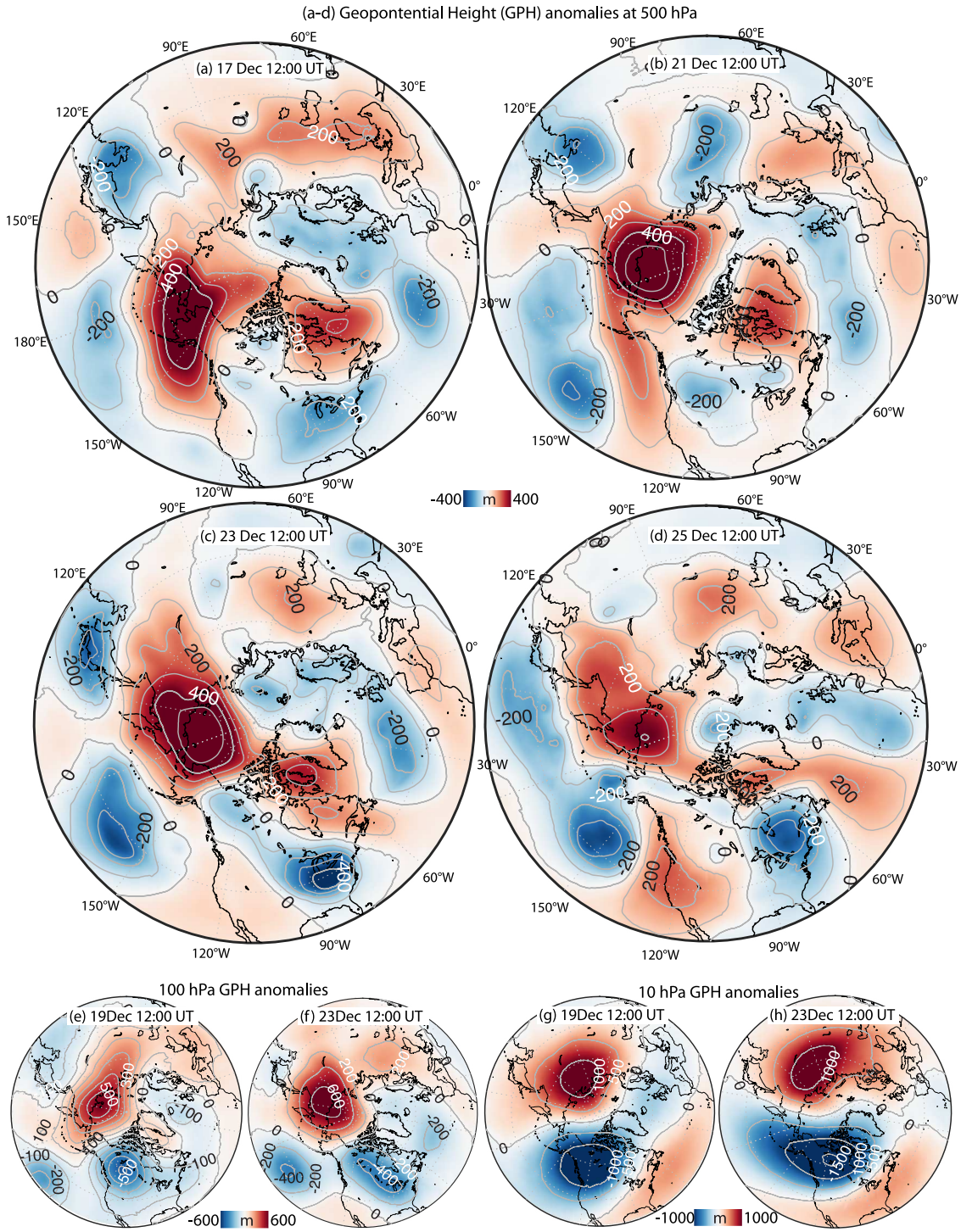

Figure 2. GPH anomalies at 12:00 UT on 17th, 21st, 23rd, and 25th of December 2022 over the polar regions derived based on ERA5 data sets at 500 hPa pressure levels. Bottom panels illustrate GPH anomalies at (e,f) 100 hPa and (g,h) 10 hPa pressure levels at selected time epochs. Contour yellow lines are GPH at 10 dam levels.

Next, Figures 3a–3d demonstrates the absolute values of horizontal winds at 4 pressure levels—750 hPa (~2.5 km), 400 hPa (~7.1 km), 250 hPa (~10 km), and 10 hPa (~26 km) from ERA5 data products at 06:00 UT on the 19th of December. GPH, depicted with contour lines, are overlaid onto the plots with the specification of values. Blue arrows illustrate wind directions. During days prior to the CAO onset, the polar jet stream shifted

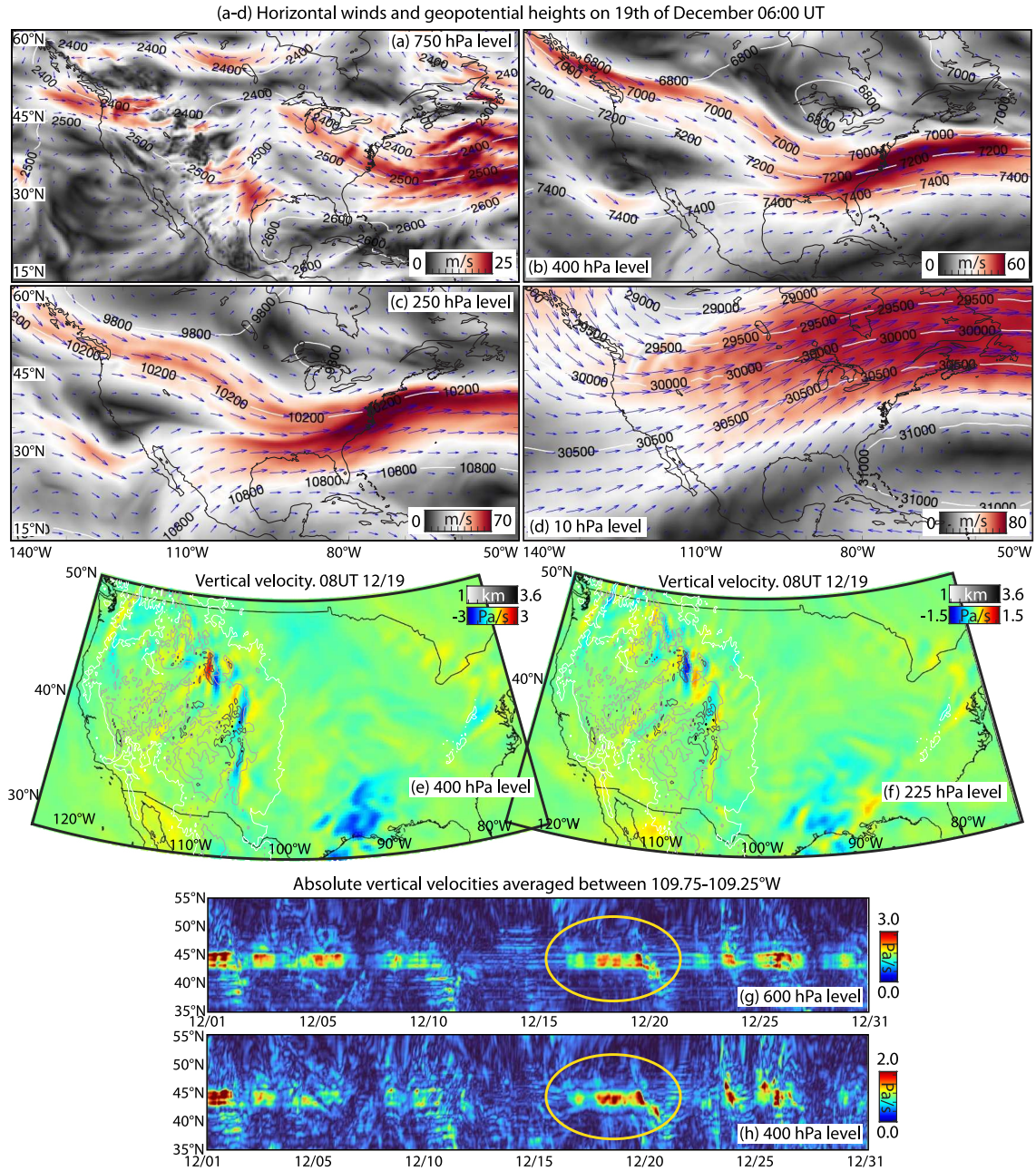

Figure 3. (a–d) Horizontal wind amplitudes and geopotential heights (illustrated in contours) at 750 hPa, 400 hPa, 250 hPa, and 10 hPa pressure levels at 06:00 UT, 19th of December 2022 retrieved from ERA5. (e,f) Vertical velocity overlaid onto the topography over CONUS at 400 and 225 hPa pressure levels at 17:00 UT, 19th of December retrieved from ERA5. The contours in panels (e) and (f) illustrate the topography with 720 m per level. (g,h) Time-latitude diagrams of absolute vertical velocities averaged over 109.5°W ± 0.25°.

toward the north-western regions of the CONUS. One may find a steep gradient in amplitudes of horizontal winds propagating in the region 45–47°N–110°W on 750–250 hPa levels. This region corresponds to the Middle Rockies, west Wyoming over Wind River and Absaroka ranges and includes mountain chains reaching 4,200 m above sea level, which could result in blocking of horizontal winds flowing across, from the west-northwest to the east (Figure 3a). Predominantly eastward winds at 750 hPa level reached values up to 26 m/s at the eastern part of Rocky Mountains, and up to ∼54 m/s and ∼62 m/s at 400 hPa and 250 hPa levels, respectively (Figures 3b and 3c). The westerlies at stratospheric heights exhibited values in the range 40–60 m/s over the region of interest, but were stronger to the northeast over Canada (Figure 3d).

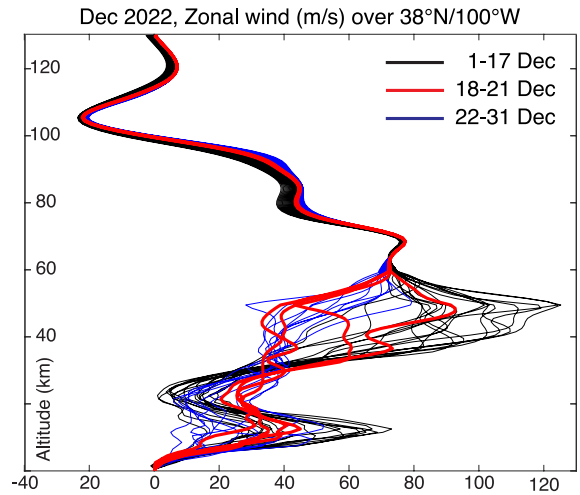

Figure 4. The altitudinal profiles of zonal winds during 1–17th (black lines), 18–21st (red lines) and 22–31st (blue lines) of December 2022 over 40°N/100°W. The profiles are based on blended MERRA-2 reanalysis below 50 km and HWM-14 empirical model above 50 km.

Vertical winds from ERA5 reanalysis at 400 hPa and 225 hPa pressure levels reached large values, ∼5–6 Pa/s, and were dominantly aligned in the meridional directions over a comparatively limited region over the east Rocky Mountains—42–45°N (Figures 3e and 3f). Their intensification is found throughout the 18–21 of December, as can be seen from Figures 3g and 3h, which illustrate latitude-time diagrams of vertical winds averaged over 109.5°W ± 0.25°. These winds exhibited quasi-stationary structures, peaking in their amplitudes on 18–20 of December, that is, prior to the CAO onset (see also the animations in the SM).

Our hypothesis that the prominent fluctuations seen in the mesosphere and the ionosphere (demonstrated in the following section) were related to sAGWs from breaking of orographic GWs generated over Rocky Mountains during 19–21 of December, is supported by the analysis of vertical profiles of zonal winds. Figure 4 illustrates zonal winds retrieved from MERRA-2 below 50 km blended with the results from the empirical wind model HWM-14 (Drob et al., 2015) at 50–130 km altitudes over the 38°N/100°W location. Orographic GWs can be critical level filtered and absorbed into the mean flow at altitudes where wind reversals occur, preventing their upward propagation. While some of the days between the 1–10 of December demonstrated comparatively strong vertical winds over the Rocky Mountains (Figures 3g and 3h), the zonal wind (Figure 4, black lines) approached zero speeds at altitudes ∼22 km so the GWs could potentially not propagate to the upper atmosphere due to critical level filtering. At the same time, the profiles during the 19th–21st of December (Figure 4, red lines) show dominant eastward winds, exhibiting values >20 m/s all up the mesopause altitudes, supporting the conclusion that there were no critical levels to impede the free propagation of GWs up to the mesosphere-lower thermosphere (MLT) region. The free propagation of these GWs would allow them to obtain large amplitudes and eventually break as they approached the critical level at mesopause (∼95 km altitudes), generating sAGWs that can propagate further into the ionosphere and induce the TIDs. Finally, although the horizontal winds after the 21st of December still exhibited strong positive values (Figure 4, blue lines), the vertical winds over the Rocky Mountains were of much smaller amplitudes (Figures 3g and 3h), potentially resulting in small amplitude (or undetectable) TIDs.

3.2. Observations of Gravity Waves

3.2.1. NASA Aqua AIRS Observations

Figures 5a–5h show the AIRS 4.3 μm BT observations between 16 and 22 of December 2022. The scans are grouped by those acquired during local day time (08-17 LT) and night time (17-08 LT) and are plotted together over the CONUS. The largest amplitude fluctuations are present over and to the east of Rocky Mountains, in particular over Great Plains (40–55°N/100–115°W) on 19th of December. They coincide with the region of the abrupt change in the tropospheric polar jet intensity (Figures 3a–3d), as well as prominent sustained vertical

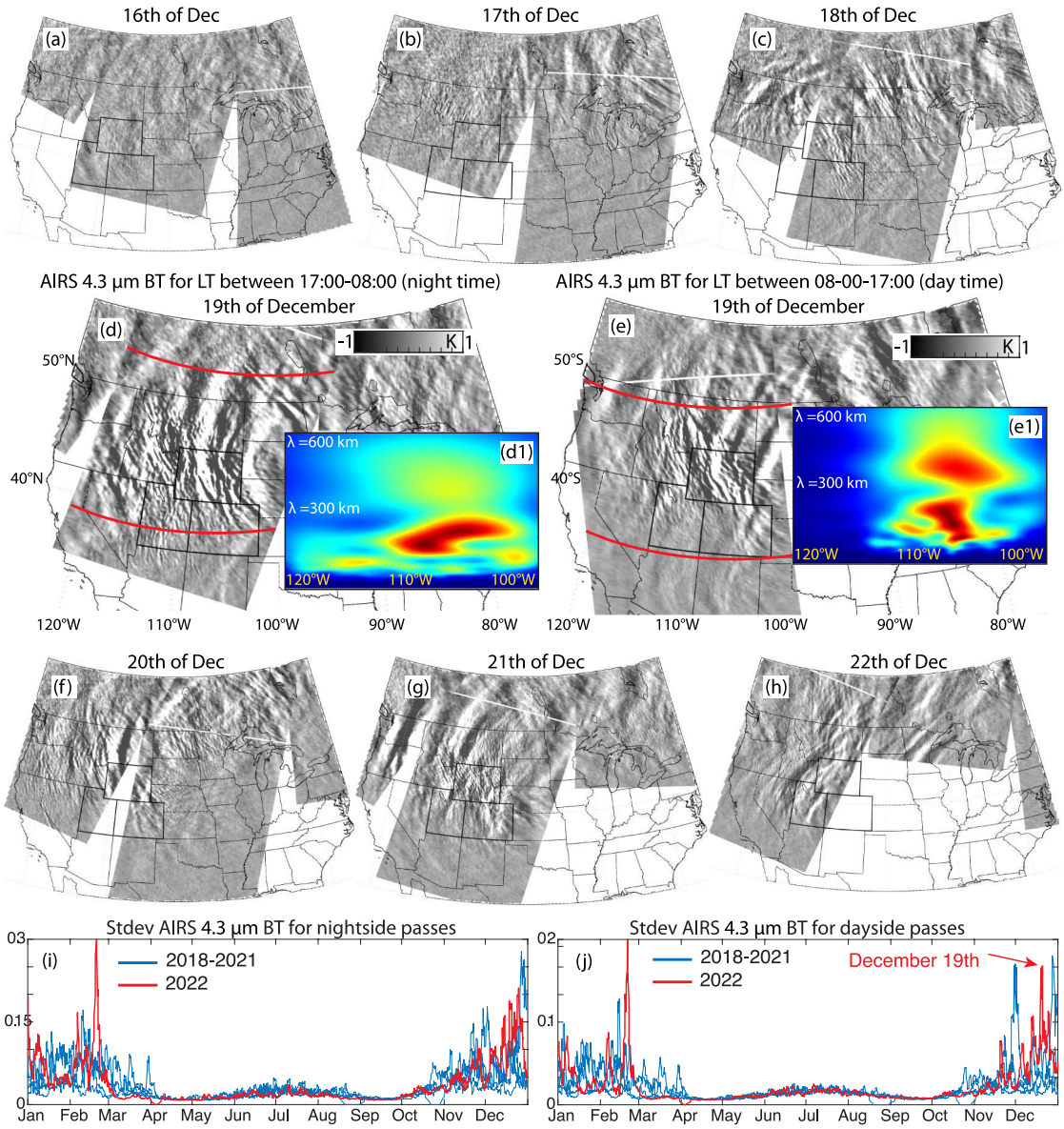

Figure 5. (a–h) Atmospheric Infrared Sounder (AIRS) 4.3 μm brightness temperature (BT) observations during 16–22 of December 2022. Except for the 19th of December, the panels demonstrate observations between 17:00-08:00 LT. The colorbars are limited to ±1 K to highlight small scale and amplitude fluctuations. Panels (d1,e1) illustrate latitude averaged wavelet power spectra of AIRS 4.3 μm BT observations between red lines shown in panels (d) and (e). (i,j) Standard derivation of AIRS 4.3 μm BT observations between 2018 and 2022 for day and night passes of the satellite.

velocities as highlighted by Figures 3e and 3f. Then, the fluctuations on 21st and 22nd of December are shifted and observed to the south and coincide with the presence of strong vertical winds over the southern part of the Rocky Mountains (see animation in the SM). The BT fluctuations increased in amplitude from the 16th December (1–3 K), peaking on the 19th December with amplitudes of 9–11 K, and then gradually weakened through to the 22nd of December (3–8 K). The slightly curved morphology, and quasi stationary nature of the wave fronts are similar to simulations (Heale et al., 2022; Lund et al., 2020) and observations (e.g., Alexander & Teitelbaum, 2011) of orographic GWs, which remained quasi-stationary for a period of several days. Figures 5d1 and 5e1 illustrate a wavelet analysis of the spatial scales present in these AIRS observations. A wavelet transform is performed as a function of longitude at each of the latitudes between the two red lines shown in panels d and e with a meridional step of 1°. The wavelet spectral power is then averaged over the latitude range denoted by the

red lines. The dominant scales of GWs detected with AIRS BT observations lie in the range of 150–280 km with another peak at ∼400 km.

The morphology of the GWs, in particular their bow shaped curvature in the meridional direction, is potentially driven by meridional shears of stratospheric zonal winds, which result in the wave elongation toward stronger westerlies (Q. Jiang et al., 2019). Indeed, as it can be seen from Figures 3a–3d, predominantly zonal winds from polar jet stream at northeast of CONUS (45–55°N) could result in eastward elongation and bending of GWs, whereas comparatively modest winds to the south (40–45°N) did not result in notable refraction of GWs (Figure 5d). We note that recent studies demonstrate that meridional asymmetry of GW shapes can also result from self-acceleration by nonlinear wave-wave and wave-mean flow interactions (Fritts et al., 2021; Heale et al., 2022).

Finally, in order to assess the apparent amplitudes of the waves during the event relative to typical conditions, we calculate the standard deviation (Stdev) of the AIRS 4.3 μm BT observations for each granule/scene (a collection of 90 × 135 pixels produced by across track swaths as the satellite nadir direction travels along its orbit for 6 min) over the CONUS for the years 2018–2022. We note that, due to lower scene temperatures in AIRS measurements in the winter as compared to the summer, there will be higher noise in the winter granules (Hoffmann et al., 2014). This means that the standard deviations of granules will be higher in winter than in summer and can contribute to the changes in the "baseline" standard deviations across the seasons. However, the local peaks in standard deviations are still a reflection of the apparent strength of wave activity on a day-to-day basis.

The resulting time series are illustrated in Figures 5i and 5j for the daytime and nighttime AIRS passes. The general trend shows high Stdev values in the winter times associated with the large jet stream winds, minima in the equinox months, when the mean stratospheric winds are weak, and a modest increase during the summer months when the westward stratospheric winds maximize. We find a sustained increase in Stdev between 16 and 22 of December 2022 before the CAO onset over CONUS. While there is a large spike in the Stdev values on the 19th December, there are also comparably large spikes on 02/13/2018, 02/10/2019, 11/30/2020, and 12/27/2021. However, none of these days includes TIDs of similar severity and duration as during the 19–21st of December 2022. We provide the vTEC fluctuation animations for these days in the SM. We also highlight that no notable convection systems were present in the northwest or north of the Great Plains during 18–22 of December 2022. We do not expect that sparsely separated systems could produce GWs of the intensity found in the AIRS observations.

3.2.2. 557.7 and 630.0 nm Airglow Observations

In this section we present 557.7 nm mesopause and 630.0 thermosphere airglow observations. Figure 6 represents difference images retrieved from the imager installed at CVO and CFS. The animations for both red and green lines for 13–24 of December 2022 are provided in the SM. We note that although airglow images are not calibrated to the absolute values, the relative values are comparable between the days presented. Thus, we use the same colorbars for all green line images and for all red line images in Figure 6.

In CVO site observations, comparatively intense fluctuations in green line emission were mostly present on the 18–19th of December (Figures 6f–6j) and some can be incidentally found during the 20–22 of December. There were only small amplitude fluctuations present on the nights prior to the CAO onset (Figures 6a–6e). Clouds during the 20–22nd could mask the fluctuations, whereas there were practically no clouds during the 19th of December. On this day, short-period and small-scale fluctuations were present during the whole ∼11 hr observation period. The fluctuations had a mostly eastward direction of propagation, whereas they were of comparatively weak amplitudes to the west. This may potentially be connected with the mostly eastward zonal winds on the 19th of December (Figure 4). The scales of fluctuations vary between 25 and 40 km of horizontal wavelength. We expect that these fluctuations may result from orographic GW breaking approaching critical level at altitudes of ∼95 km, as can be seen from Figure 4.

In comparison, the most prominent fluctuations in red line were present only between 2 and 3 UT on the 19th of December in CVO site observations. They had preferential westward and southwestward directions of propagation (Figures 6q–6s). The horizontal wavelengths of dominant fluctuations are estimated as 160–250 km. Interestingly, the turbulence-like dynamics were also present in these observations between 5 and 9 UT, although

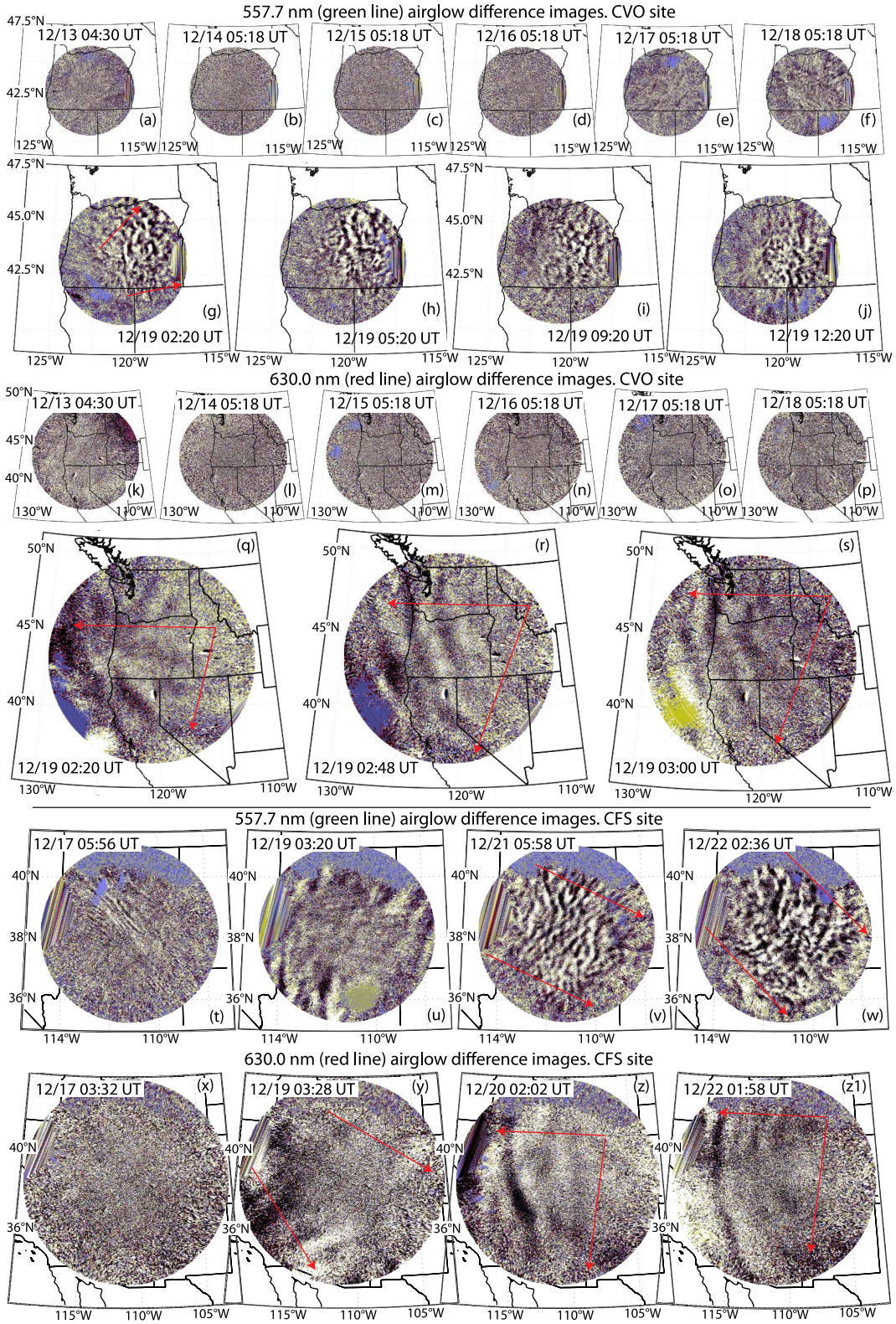

Figure 6. 557.7 and 630.0 nm airglow emission difference imager from the imagers installed at (a–s) Christmas Valley Observatory (CVO) (43.2°N/120.7°W) during 13–19th of December 2022 from CVO site and (t–z1) Capitol Reef Field Station site during 17–22nd of December 2022.

with comparatively small amplitudes (see animations in the SM). Again, there were only small amplitude fluctuations present on the nights prior to the CAO onset in this emission line (Figures 6k–6p).

At the same time, the green line observations from CFS site demonstrate comparatively weak fluctuations during 17–19th of December (Figures 6t and 6u), but the strongest fluctuations during 21 and 22nd of December (Figures 6v and 6w). Their morphology is similar to the one from CVO site imager observations, that is, short-period and small-scale fluctuations, in this case propagating from the southern part of the Rocky Mountains. The delay between the observations of fluctuations at CVO and CFS sites' imagers is similar to the presence of fluctuations observed from AIRS 4.3 μm BT observations, which demonstrated the strongest values to the north of Rocky Mountains on 18–19th of December, and the strongest fluctuations to the south of Rocky Mountains on 21–22nd of December, as discussed above. For red line, CFS site observations suggest southeastward apparently propagating fluctuations starting from 19th of December, potentially from the region northeast of Rocky Mountains (Figure 6y). During 20–22nd of December, the comparable fluctuations propagated southwestward from the region southeast of Rocky Mountains, in a similar manner as found from CVO site observations (Figures 6z and 6z1). The scales of fluctuations from CFS site 557.7 and 630.0 nm observations are very similar to those reported above for the site CVO, potentially pointing to the same source.

3.3. Traveling Ionospheric Disturbances

3.3.1. GNSS Total Electron Content Observations

The snapshots of GNSS vTEC observations over the CONUS for the 19–22 of December are illustrated in Figure 7. vTEC are mapped with their respective IPP locations, excluding observations with elevation angles of line-of-sights between GNSS receivers and satellites (LOS) below 10°. Panels a–g show 15/30 s sampling rate vTEC processed with an 8–30 min band-pass filter. Panels h–j include 10 min high-pass filtered 1 s sampling rate vTEC observations, from GNSS receivers mostly confined over the western part of the CONUS. For consistency, we restricted our analysis of TIDs to local day times only, that is, between 16 and 02 UT. The vTEC animations for full days between 18 and 27 of December are provided in the SM.

Concentrically propagating TIDs emanating from the region east of the Rocky Mountains started to be observable on the 18th of December at 00–02 UT (Figure 7a). The largest in amplitude and most consistent concentric fluctuations are detectable starting from the 19th of December (Figures 7b and 7c). During local evening of the 19th of December, the TIDs were still present, but exhibited more complex shapes and dynamics (Figure 7d). The TIDs during 20th and 21st of December were comparable to those on the 19th of December, with concentric fluctuations propagating from east of the Rocky Mountains (Figures 7e and 7f). Beyond the 18–21st, only common planar-looking TIDs (during local day times), propagating northwest-southeast, were present (Figure 7g and animations in the SM). On average, the periods of TIDs are estimated to range from 13 to 18 min and their amplitudes during the 19th and 20th of December reached 0.7 TECu, whereas they were in the range of 0.1–0.3 TECu during other days. We also highlight the presence of short period TIDs during the 18–21 of December of ∼3–5 min periods and amplitudes ranging from 0.02 to 0.25 TECu (Figures 7h–7j). They apparently originated from the same area as TIDs of longer periods—east of the Rocky Mountains. The propagation of short-scale TIDs is predominantly equatorward, apparently confined by magnetic field lines. Their characteristics and the dynamics suggest compressible modes of AGWs as their sources, potentially generated from orographic GW breaking.

Next, Figure 8 illustrates 15/30 s sampling rate vTEC observations processed with a 10 min high-pass filter (panel a) and 5–40 min band-pass filter (panel b) as longitude-time diagrams along a latitude of 45°N between the 11th and 27th of December. The Stdev AIRS 4.3 μm BT values from Figure 5j (black lines), as well as vertical wind values (red lines) as shown above in Figures 3g and 3h but averaged over 42–45°N, are overlaid on these plots. To avoid ionospheric electron density daily variability impacts on the amplitudes of TIDs in this analysis, we demonstrate the observations only during local day time, framed around 16–24 UT. First, the AIRS Stdev 4.3 μm BT time series highlight the strongest GWs observed during the 19th of December. The peak in the AIRS Stdev 4.3 μm BT exactly coincides with the strongest amplitude TIDs (both short period 3–5 min and longer period 13–18 min ones) on 19th of December. Similarly, vertical winds exhibited their highest values during the 19–21st of December, matching the presence of concentric TIDs propagating over the CONUS. Again, although other days exhibited comparatively high values of AIRS Stdev 4.3 μm BT or vertical winds, for example, 24–25th of December, none of them included TIDs of amplitudes and consistency as found during 19–21st of December.

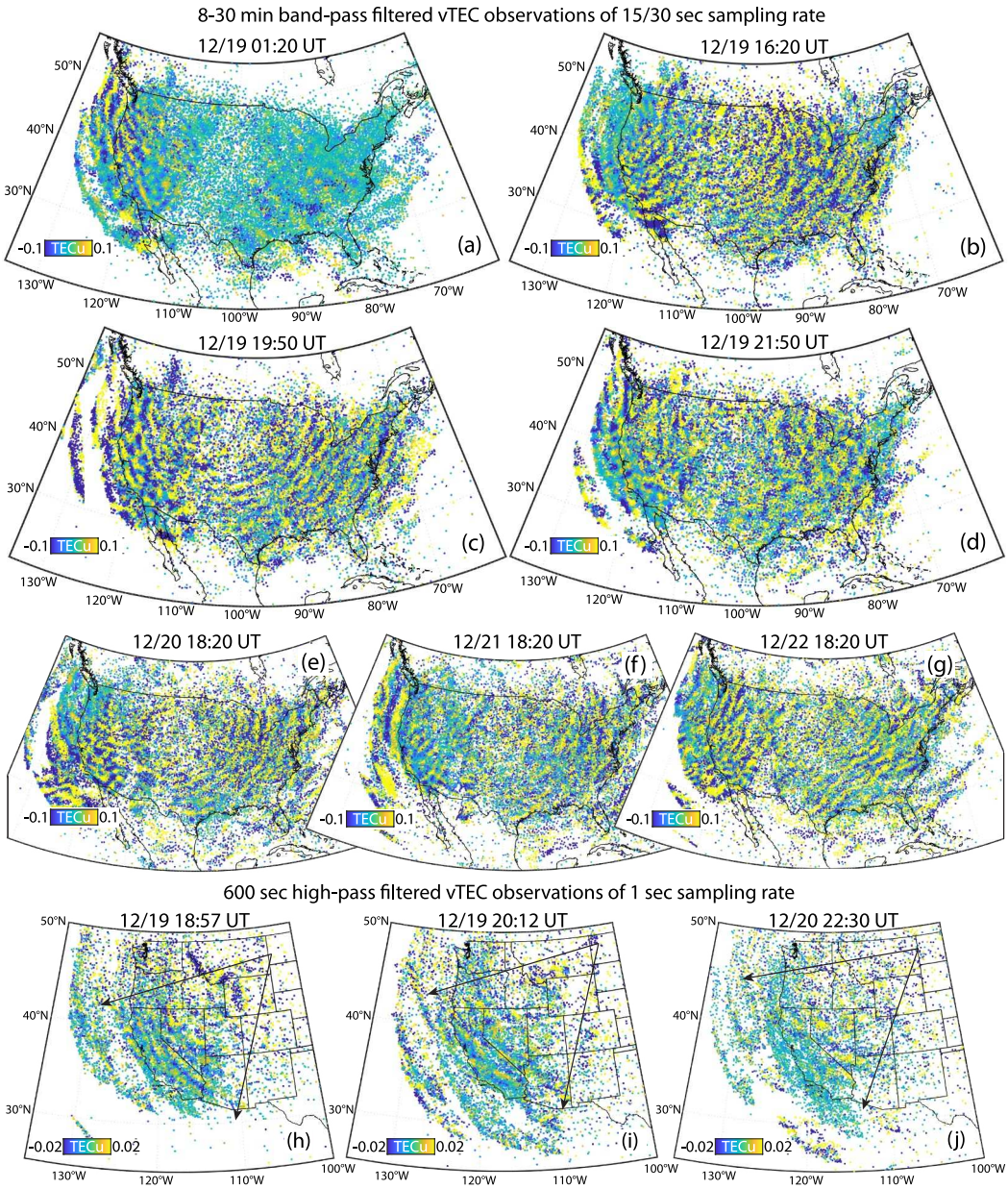

Figure 7. The snapshots of vTEC mapped with respective ionospheric pierce point locations over North America between the 19–22 of December and processed with (a–g) 8–30 min band-pass filter applied to 15/30 s sampling rate observations, and (h–j) 10 min high-pass filter applied to 1 s sampling rate observations. The colorbars on illustrations are over-saturated to highlight small amplitude and small-scale traveling ionospheric disturbances.

To better understand the morphology of short period TIDs, Figures 8c and 8d illustrate the time-distance diagrams of 10 min high-pass filtered vTEC observations. The distance is calculated from 48°N/105°W - the region of apparent excitation of short-period TIDs (see Figures 7e–7g). During the 19–20th of December, these TIDs had amplitudes up to 0.25 TECu and periods in the range 3–5 min, suggesting AGWs as their possible source. The phase speeds of them are estimated as ∼1.3 km/s. Likewise, Figures 8e and 8f illustrates time-distance diagrams of 8–30 min band-pass filtered vTEC from the position 45°N/100°W, which roughly corresponds to apparent origin location of longer-period TIDs. The observations are chosen only to the south from the position. The estimated phase speeds of the TIDs are ∼210 m/s on average, although some TIDs exhibited slower speeds, of 170 or 100 m/s. As mentioned earlier, the periods of these TIDs were in the range 13–18 min. Such variability of

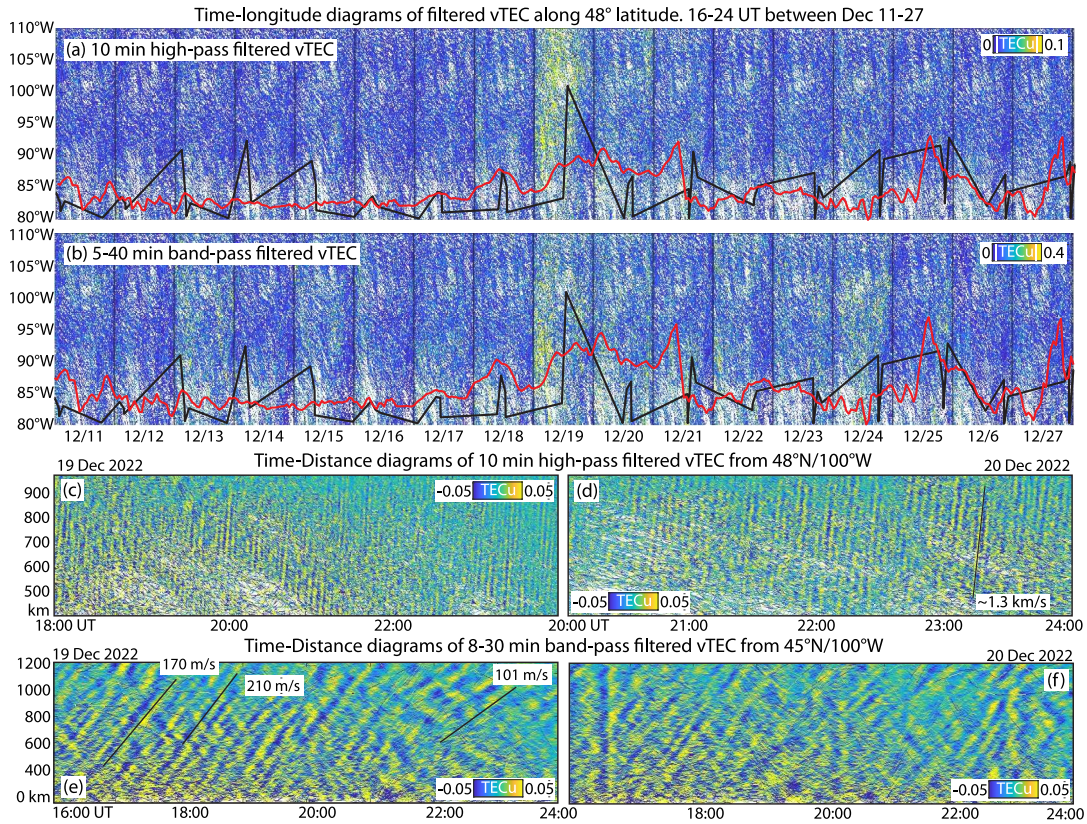

Figure 8. Time-longitude diagrams of 15/30 s sampling rate vTEC along 48°N processed with (a) 10 min high-pass and (b) 5–40 min band-pass filters during 11–27 of December 2022. The absolute values of vTEC fluctuations are shown. The diagrams represent observations for 16–24 UT of each day. Atmospheric Infrared Sounder 4.3 μm brightness temperature standard deviation (black lines) and ERA5 reanalysis vertical winds averaged over 42–45°N (red lines) are overlaid to these plots. Bottom panels illustrate time-distance diagrams of 30 s sampling rate vTEC processed with (c)–(d) 10 min high-pass filter (the distance is calculated from 48°N/100°W) and (e)–(f) 8–30 min band-pass filter (the distance is calculated from 45°N/104°W).

periods and speeds of TIDs highlights the complexity of their sources - sAGWs, which may exhibit broad spectral characteristics.

3.3.2. SuperDARN Observations

Recent studies show that the observations of TIDs in GNSS TEC match and can be supported by observations from SuperDARN. Kelley et al. (2023) demonstrated that geomagnetic storm-time electrified TIDs were broadly consistent in their characteristics between the data sets. Similar wavelet spectra were reported for subauroral polarization stream fine structures between SuperDARN and TEC observations by Makarevich and Bristow (2014). J. Zhang et al. (2022) suggested that the propagation direction and apparent horizontal phase velocity of fronts of ionospheric fluctuations observed by the SuperDARN radars were consistent with the observations based on the TEC during the 2022 Honga-Tonga volcano eruption. However, it is not yet clear if atmospheric wave-driven TIDs, as investigated here, can be effectively captured by SuperDARN data sets and if so, infer comparable periods and speeds of propagation.

In addition to the GNSS TEC, we analyzed observations from the relevant mid-latitude SuperDARN radars—Fort Hays East (FHE) and Fort Hays West (FHW). The location of these receivers and their FOVs are shown in Figure 9, along with the received power at 17 UT on 20th of December. Using a virtual height model, the range gates corresponding to the measured power can be used to approximate the location of the measurements. We use daytime GS measurements, which manifest as wave-like signatures in the range-time-intensity plots resulting from focusing and defocusing of the reflected SuperDARN beam (Frissell et al., 2014). Using the approximate location of the measurements, and by combining the FHE and FHW observations for all beams, we construct

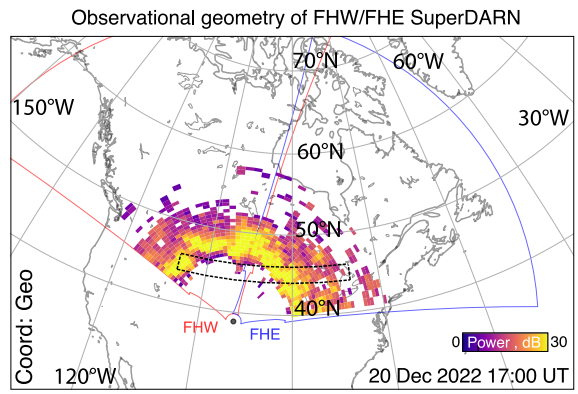

Figure 9. Observational geometry for the Fort Hays West and Fort Hays East Super Dual Auroral Radar Network radars are shown along with measured power at 17 UT on 20th of December.

time-distance plots, allowing for further comparisons of the ionospheric footprint of the TIDs observed in GNSS TEC.

The comparisons of GNSS TEC and SuperDARN data sets are illustrated in Figure 10 through the time-longitude diagrams along 48°N (indicated on specific panels) for the 20–22 of December. Panels a, d and g show vTEC observations processed with an 8–30 min band-pass filter, while panels b, e and h demonstrate the SuperDARN power in a similar arrangement. In particular, for SuperDARN we calculate time-longitude diagrams averaging power observations in the range ±0.5° from the respective latitude chosen for vTEC observations. For illustrative purposes, we also overlay the SuperDARN and vTEC perturbations for each day in panels c, f and i. The comparison is made for 16–24 UT, when TIDs in TEC of interest are clearly discernible.

We find that fluctuations in both observations match in their apparent phase speeds, which lie in the range of ∼200–240 m/s and periods, which are of ∼13–18 min. The phases of the fluctuations agree closely for the 20th and 21st of December between 16 and 22 UT (Figures 10c,f). This co-location demonstrates a high-level of agreement of fluctuations derived based on two different observational techniques. We found that the change of ionospheric shell height for the calculation IPP locations of vTEC observations to 250 km (which is used for this exercise and Figure 10), in comparison with earlier demonstrated 300 km altitude as ionospheric shell height (e.g., Figure 7), provides a better agreement with SuperDARN observations, potentially suggesting that the TID detections in SuperDARN predominantly result from the altitude below 300 km. Furthermore, the approximate location of the SuperDARN TIDs were found to be ∼264 km based on an average of three virtual height models (Chisham et al., 2008; Thomas & Shepherd, 2022), which also agrees well with the choice of the ionospheric shell height at 250 km, and confirms that the TIDs were present in the F-region.

4. Discussion and Conclusion

The North American region is known for the presence of various sources of GWs. The western part of the CONUS is a region of MW activity generated by wind flows over the Rocky Mountains (Dean-Day et al., 1998; J. H. Jiang et al., 2004; Ralph et al., 1999); cross-mountain flows over Appalachian and Greenland are also sources of MWs (Lyapustin et al., 2014; Wu & Zhang, 2004; F. Zhang et al., 2013); the variability of polar jet stream, for example, jet exit region at northwest Atlantic, is another area of GW activity (Harvey et al., 2023; F. Zhang et al., 2013). Important sources of GWs, particularly over CONUS, are weather events, such as tornadoes, thunderstorms and hurricanes, that may produce long-lasting atmospheric disturbances. The propagation of GWs to ionospheric heights, both in the form of primary waves excited in the troposphere or sAGWs from the breaking of primary waves at different altitudes, leads to the generation of TIDs of various scales (Azeem, 2021; Chen et al., 2022; Nishioka et al., 2013).

Another important source of atmospheric waves over North America is connected with a weakening of the polar vortex, what commonly leads to sudden stratospheric warmings (SSWs). Major SSWs may markedly impact thermospheric meridional wind structures, which in turn modify thermospheric circulation or induce plasma

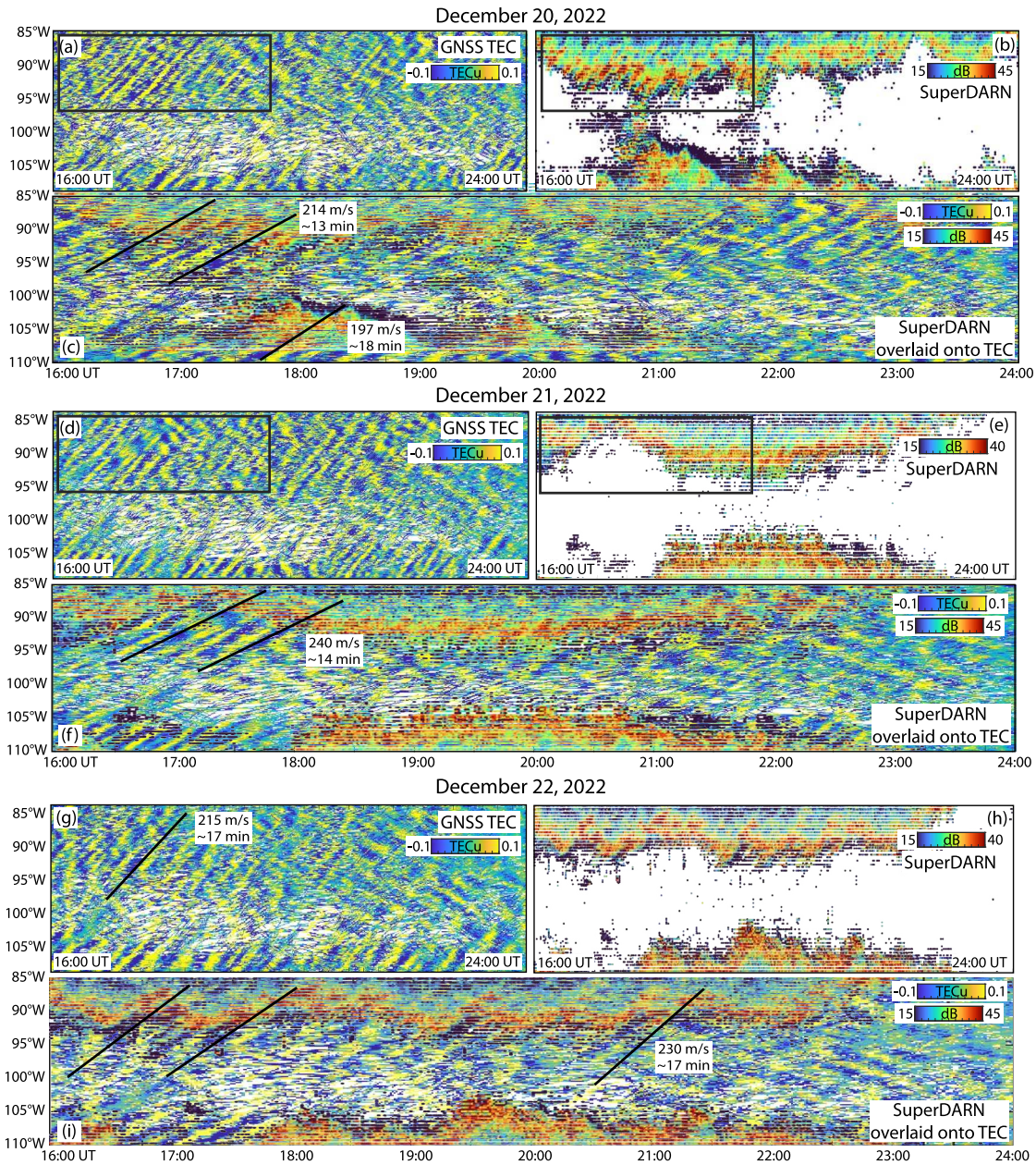

Figure 10. Time-longitude diagrams of 8–30 min band-pass filtered vTEC observations along (a–c) 48°N and (d–i) 45°N and Super Dual Auroral Radar Network (SuperDARN) power observations from the Fort Hays West and Fort Hays East transmitters. For SuperDARN, the diagrams are calculated by averaging power observations in the range ±0.5° from the respective latitude. For each of day, Global Navigation Satellite System (GNSS) total electron content (TEC) is demonstrated in the left panel and SuperDARN is in the right panel of the first row. The second row includes SuperDARN observations overlaid onto GNSS TEC observations.

redistribution in the ionosphere (Jones et al., 2023; Miyoshi et al., 2015). At the same time, the studies demonstrate that although SSWs lead to the distortion of jet stream, they result in rather reduction of GW activity in the atmosphere from the weakening of horizontal winds and inhibiting the GWs to propagate to the upper atmosphere. It is, however, worth noting that such dynamics is commonly observed during major SSWs and further studies are required to better understand the role of minor SSWs (or those resembling SSWs by their dynamics) in generation GWs over various regions of North America (Goncharenko et al., 2021).

The following paragraph presents a summary of the main outcomes of this study. The event presented in our case study is unique since it demonstrates the deep coupling of GWs and TIDs connected to CAO forcing conditions.

The analysis of observations suggests that the Alaskan ridge circulation, prior to CAO's onset over CONUS, led to the distortion of tropospheric polar vortex and the shifting of the tropospheric polar jet stream southward, which then impinged upon the Rocky Mountains. We suggest that this wind flow over the Rocky Mountains generated significant amplitude MWs as evidenced by the presence of sustained vertical velocities in ERA5 reanalysis data in the troposphere and quasi-stationary, planar wave structures in AIRS data in the stratosphere. Based upon analysis of the ambient winds, these MWs could propagate freely up to the mesopause region where the zonal wind decreases toward zero. The decreasing winds could refract MWs to smaller vertical wavelengths and cause them to break, generating sAGWs. This is supported by 557.7 nm airglow data which shows the presence of turbulent like structures in MLT region. The sAGWs generated by the MW breaking could continue to propagate upward and induce very short period TIDs (3–5 min) and the semi-concentric TIDs (8–30 min) seen in GNSS TEC and SuperDARN data. This mechanism, and transition from MW to semi-concentric sAGWs in the MLT has been demonstrated in previous data-guided and modeling studies (Bramberger et al., 2017; Heale et al., 2022; Lund et al., 2020; Vadas et al., 2019).

In consideration of wave source that could contribute to the TIDs we report in this paper, modeling results support the presence of such concentric sAGWs emerging in MLT due to MW breaking below mesopause. Similarly, some observed GWs could be generated from the complex polar jet stream dynamics itself during the event or the interaction between the MWs and the jet stream. While these mechanisms are plausible, the relative contribution of these types of GW sources on the overall spectrum of observed TIDs is impossible to ascertain without a detailed modeling study.

We also demonstrated that the observations of TIDs in SuperDARN measurements, that result from atmospheric waves, are sufficiently consistent with vTEC observations. This provides opportunities for the use of SuperDARN data sets for the analysis of comparatively small amplitude (0.05–0.7 TECu) and short-period TIDs, the detection of which can be limited with other ground-based remote and in-situ observations. Furthermore, SuperDARN observations provide an information on the approximate altitudinal location of the observed TIDs, based on the absolute range traveled by the transmitted HF rays. Since the TID characteristics are comparable across TEC and SuperDARN observations, and since SuperDARN range gate numbers for this event suggest GS after a F-region reflection from an altitude of 264 km, we can infer that both measurements observe the same TID in the F-region.

To summarize, the most important finding of this study is that the dynamics relating to CAOs over the CONUS, including distortion of tropospheric polar vortex and polar jet stream shifting southward, may lead to the generation of large amplitude MWs. The MW propagation to the middle and upper atmosphere can lead to wave breaking and the generation of sAGWs, which can induce comparatively large disturbances in the ionospheric plasma densities over the whole CONUS for several days. This, in addition to wave associated momentum and energy deposition in the thermosphere, may also markedly redistribute ionospheric plasma and lead to notable electrodynamics effects. This case study supports mechanisms demonstrated in previous modeling studies (Heale et al., 2022; Lund et al., 2020; Vadas et al., 2019) and would benefit from future modeling efforts of such events to better understand the dynamics of MWs over North America region and their impacts on the upper atmosphere. Likewise, future studies may target the understanding the role of polar vortex dynamics that favor or preclude the propagation of MWs to the upper atmosphere and ionosphere over CONUS (Goncharenko et al., 2021; Harvey et al., 2018), also targeting the understanding of the statistical significance and occurrence frequency of events such as the one presented in this paper.

Data Availability Statement

The horizontal winds, vertical velocities and geopotential height, as well as 2-m temperature data used for the climotological context of the event in the study are available at Copernicus Climate Change Service (C3S) Climate Data Store via https://doi.org/10.24381/cds.bd0915c6 (Hersbach et al., 2023) with Copernicus Products Licence. MERRA-2 horizontal winds used for the investigation of wind flows during December 2022 in the study are available at NASA Goddard Earth Sciences Data and Information Services Center (DISC) via https://doi.org/10.5067/QBZ6MG944HW0 (Global Modeling and Assimilation Office (GMAO), 2015) with public access. SuperDARN power observations used for the analysis of traveling ionospheric disturbances in the study are available at Virginia Tech data server via http://vt.superdarn.org/ with public access. The radars are

maintained and operated by Dartmouth College under support by NSF Grant AGS-1341925. We acknowledge the use of SuperDARN data. SuperDARN is a network of radars funded by national scientific funding agencies of Australia, Canada, China, France, Italy, Japan, Norway, South Africa, the United Kingdom, and the United States of America. AIRS BT observations used for the investigation of GW-driven fluctuations in the study are available at Jülich Supercomputing Centre SLCS Data Repository via https://datapub.fz-juelich.de/slcs/airs/gravity_waves/html/cal_2017.html with CC BY 4.0 DEED license. 557.7 and 630 nm airglow emission observations used for the investigation of GW-driven fluctuations in the study are available at MANGO web-site via https://www.mangonetwork.org/mango/v1 with public access. Midlatitude Allsky-imaging Network for GeoSpace Observations network operated by SRI International with support from NSF award AGS-1933013. GNSS TEC observations used for the investigation of traveling ionospheric disturbances in the study are available at (a)Scripps Orbit and Permanent Array Center via http://sopac-csrc.ucsd.edu/index.php/gnss/ with public access, (b) The National Aeronautics and Space Administration the Crustal Dynamics Data Information System (Noll, 2010) via https://cddis.nasa.gov/archive/gnss/data/daily/ with public access, (c) National Oceanic and Atmospheric Administration's National Geodetic Survey NGS via https://geodesy.noaa.gov/CORS/ with public access and GAGE Facility operated by UNAVCO, Inc. via https://www.unavco.org/data/gps-gnss/gps-gnss.html with public access. GAGE Facility, operated by UNAVCO, Inc., is supported by the National Science Foundation and the U.S. Geological Survey under NSF Cooperative Agreement EAR-1724794. pyDARN v4.0 used for the analyzing the SuperDARN data sets is preserved at https://zenodo.org/records/10452339, available via LGPL v3 License. The Supplemental Materials are publicly available through ERAU's Data Commons: https://datacommons.erau.edu/datasets/v7342nzsm3/1.

Acknowledgments
This research is supported by NASA LWS 80NSSC22K1022. Except Inchin P.A., all authors are listed alphabetically. SC also thanks to the National Science Foundation and the NASA for support under Grants AGS-1935110 and 80NSSC20K1380, respectively.

References

Alexander, M. J., & Teitelbaum, H. (2011). Three-dimensional properties of Andes mountain waves observed by satellite: A case study. *Journal of Geophysical Research*, *116*(D23). https://doi.org/10.1029/2011JD016151

Azeem, I. (2021). Spectral asymmetry of near-concentric traveling ionospheric disturbances due to Doppler-shifted atmospheric gravity waves. *Frontiers in Astronomy and Space Sciences*, *8*, 690480. https://doi.org/10.3389/fspas.2021.690480

Bhatt, A. N., Harding, B. J., Makela, J. J., Navarro, L., Lamarche, L. J., Valentic, T., et al. (2023). MANGO: An optical network to study the dynamics of the Earth's upper atmosphere. *Journal of Geophysical Research: Space Physics*, *128*(10), e2023JA031589. https://doi.org/10.1029/2023JA031589

Birner, T., & Albers, J. R. (2017). Sudden stratospheric warmings and anomalous upward wave activity flux. *SOLA*, *13A*(Special Edition), 8–12. https://doi.org/10.2151/sola.13A-002

Bossert, K., Kruse, C. G., Heale, C. J., Fritts, D. C., Williams, B. P., Snively, J. B., et al. (2017). Secondary gravity wave generation over New Zealand during the DEEPWAVE campaign. *Journal of Geophysical Research: Atmospheres*, *122*(15), 7834–7850. https://doi.org/10.1002/2016JD026079

Bramberger, M., Dörnbrack, A., Bossert, K., Ehard, B., Fritts, D. C., Kaifler, B., et al. (2017). Does strong tropospheric forcing cause large-amplitude mesospheric gravity waves? A DEEPWAVE case study. *Journal of Geophysical Research: Atmospheres*, *122*(21), 11422–-11443. https://doi.org/10.1002/2017JD027371

Cellitti, M. P., Walsh, J. E., Rauber, R. M., & Portis, D. H. (2006). Extreme cold air outbreaks over the United States, the polar vortex, and the large-scale circulation. *Journal of Geophysical Research*, *111*(D2). https://doi.org/10.1029/2005JD006273

Chen, Y., Yue, D., Zhai, C., & Zhang, S.-R. (2022). Detection and three-dimensional reconstruction of concentric traveling ionosphere disturbances induced by Hurricane Matthew on 7 October 2016. *Journal of Geophysical Research: Space Physics*, *127*(12), e2022JA030690. https://doi.org/10.1029/2022JA030690

Chisham, G., Lester, M., Milan, S. E., Freeman, M. P., Bristow, W. A., Grocott, A., et al. (2007). A Decade of the Super Dual Auroral Radar Network (SuperDARN): Scientific achievements, new techniques and future directions. *Surveys in Geophysics*, *28*(1), 33–109. https://doi.org/10.1007/s10712-007-9017-8

Chisham, G., Yeoman, T. K., & Sofko, G. (2008). Mapping ionospheric backscatter measured by the superdarn hf radars–part 1: A new empirical virtual height model. *Annales Geophysicae*, *26*(4), 823–841. https://doi.org/10.5194/angeo-26-823-2008

Chou, M.-Y., Yue, J., Sassi, F., McDonald, S., Tate, J., Pedatella, N., et al. (2023). Modeling the day-to-day variability of midnight equatorial plasma bubbles with SAMI3/SD-WACCM-X. *Journal of Geophysical Research: Space Physics*, *128*(5), e2023JA031585. https://doi.org/10.1029/2023JA031585

Dean-Day, J., Chan, K. R., Bowen, S. W., Bui, T. P., Gary, B. L., & Mahoney, M. J. (1998). Dynamics of Rocky Mountain lee waves observed during SUCCESS. *Geophysical Research Letters*, *25*(9), 1351–1354. https://doi.org/10.1029/98GL01004

Drob, D. P., Emmert, J. T., Meriwether, J. W., Makela, J. J., Doornbos, E., Conde, M., et al. (2015). An update to the Horizontal Wind Model (HWM): The quiet time thermosphere. *Earth and Space Science*, *2*(7), 301–319. https://doi.org/10.1002/2014EA000089

Eckermann, S. D., & Preusse, P. (1999). Global measurements of stratospheric mountain waves from space. *Science*, *286*(5444), 1534–1537.

Ehard, B., Kaifler, B., Dörnbrack, A., Preusse, P., Eckermann, S. D., Bramberger, M., et al. (2017). Horizontal propagation of large-amplitude mountain waves into the polar night jet. *Journal of Geophysical Research: Atmospheres*, *122*(3), 1423–1436. https://doi.org/10.1002/2016JD025621

Frissell, N. A., Baker, J., Ruohoniemi, J. M., Gerrard, A. J., Miller, E. S., Marini, J. P., et al. (2014). Climatology of medium-scale traveling ionospheric disturbances observed by the midlatitude Blackstone SuperDARN radar. *Journal of Geophysical Research: Space Physics*, *119*(9), 7679–7697. https://doi.org/10.1002/2014JA019870

Fritts, D. C., & Alexander, M. J. (2003). Gravity wave dynamics and effects in the middle atmosphere. *Reviews of Geophysics*, *41*(1). https://doi.org/10.1029/2001RG000106

Fritts, D. C., Lund, T. S., Wan, K., & Liu, H.-L. (2021). Numerical simulation of mountain waves over the southern Andes. Part II: Momentum fluxes and wave–mean-flow interactions. *Journal of the Atmospheric Sciences*, *78*(10), 3069–3088. https://doi.org/10.1175/JAS-D-20-0207.1

Garcia, R. R., & Solomon, S. (1985). The effect of breaking gravity waves on the dynamics and chemical composition of the mesosphere and lower thermosphere. *Journal of Geophysical Research*, *90*(D2), 3850–3868. https://doi.org/10.1029/JD090iD02p03850

Global Modeling and Assimilation Office (GMAO). (2015). MERRA-2 3D IAU State, Meteorology Instantaneous 3-hourly (p-coord, 0.625x0.5L42). [Dataset]. https://doi.org/10.5067/QBZ6MG944HW0

Goncharenko, L. P., Harvey, V. L., Liu, H., & Pedatella, N. M. (2021). Sudden stratospheric warming impacts on the ionosphere–thermosphere system. In *Ionosphere dynamics and applications* (pp. 369–400). American Geophysical Union (AGU). https://doi.org/10.1002/9781119815617.ch16

Greenwald, R. A., Baker, K. B., Hutchins, R. A., & Hanuise, C. (1985). An HF phased-array radar for studying small-scale structure in the high-latitude ionosphere. *Radio Science*, *20*(1), 63–79. https://doi.org/10.1029/RS020i001p00063

Grotjahn, R., Black, R., Leung, R., Wehner, M. F., Barlow, M., Bosilovich, M., et al. (2016). North American extreme temperature events and related large scale meteorological patterns: A review of statistical methods, dynamics, modeling, and trends. *Climate Dynamics*, *46*(3–4), 1151–1184. https://doi.org/10.1007/s00382-015-2638-6

Harvey, V. L., Randall, C. E., Goncharenko, L., Becker, E., & France, J. (2018). On the upward extension of the polar vortices into the mesosphere. *Journal of Geophysical Research: Atmospheres*, *123*(17), 9171–9191. https://doi.org/10.1029/2018JD028815

Harvey, V. L., Randall, C. E., Goncharenko, L. P., Becker, E., Forbes, J. M., Carstens, J., et al. (2023). CIPS observations of gravity wave activity at the edge of the polar vortices and coupling to the ionosphere. *Journal of Geophysical Research: Atmospheres*, *128*(12), e2023JD038827. https://doi.org/10.1029/2023JD038827

Heale, C. J., Bossert, K., & Vadas, S. L. (2022). 3D numerical simulation of secondary wave generation from mountain wave breaking over europe. *Journal of Geophysical Research: Atmospheres*, *127*(5), e2021JD035413. https://doi.org/10.1029/2021JD035413

Heale, C. J., Bossert, K., Vadas, S. L., Hoffmann, L., Dörnbrack, A., Stober, G., et al. (2020). Secondary gravity waves generated by breaking mountain waves over Europe. *Journal of Geophysical Research: Atmospheres*, *125*(5), e2019JD031662. https://doi.org/10.1029/2019JD031662

Hersbach, H., Bell, B., Berrisford, P., Biavati, G., Horányi, A., Muñoz Sabater, J., et al. (2023). ERA5 hourly data on pressure levels from 1940 to present. [Dataset]. https://doi.org/10.24381/cds.bd0915c6

Hertzog, A., Boccara, G., Vincent, R. A., Vial, F., & Cocquerez, P. (2008). Estimation of gravity wave momentum flux and phase speeds from quasi-Lagrangian stratospheric balloon flights. Part II: Results from the Vorcore campaign in Antarctica. *Journal of the Atmospheric Sciences*, *65*(10), 3056–3070. https://doi.org/10.1175/2008JAS2710.1

Hickey, M., & Cole, K. (1988). A numerical model for gravity wave dissipation in the thermosphere. *Journal of Atmospheric and Terrestrial Physics*, *50*(8), 689–697. https://doi.org/10.1016/0021-9169(88)90032-3

Hines, C. O. (1960). Internal atmospheric gravity waves at ionospheric heights. *Canadian Journal of Physics*, *38*(11), 1441–1481. https://doi.org/10.1139/p60-150

Hoffmann, L., Alexander, M. J., Clerbaux, C., Grimsdell, A. W., Meyer, C. I., Rößler, T., & Tournier, B. (2014). Intercomparison of stratospheric gravity wave observations with AIRS and IASI. *Atmospheric Measurement Techniques*, *7*(12), 4517–4537. https://doi.org/10.5194/amt-7-4517-2014

Hoffmann, L., Xue, X., & Alexander, M. J. (2013). A global view of stratospheric gravity wave hotspots located with Atmospheric Infrared Sounder observations. *Journal of Geophysical Research: Atmospheres*, *118*(2), 416–434. https://doi.org/10.1029/2012JD018658

Holt, L. A., Alexander, M. J., Coy, L., Liu, C., Molod, A., Putman, W., & Pawson, S. (2017). An evaluation of gravity waves and gravity wave sources in the Southern Hemisphere in a 7 km global climate simulation. *Quarterly Journal of the Royal Meteorological Society*, *143*(707), 2481–2495. https://doi.org/10.1002/qj.3101

Huba, J. D., & Liu, H.-L. (2020). Global modeling of equatorial spread F with SAMI3/WACCM-X. *Geophysical Research Letters*, *47*(14), e2020GL088258. https://doi.org/10.1029/2020GL088258

Inchin, P., Bhatt, A., Cummer, S., Eckermann, S., Harding, B., Kuhl, D., et al. (2023). Multi-layer evolution of acoustic-gravity waves and ionospheric disturbances over the United States after the 2022 Hunga Tonga volcano eruption. *AGU Advances*, *4*(6), e2023AV000870. https://doi.org/10.1029/2023AV000870

Inchin, P., Heale, C., Snively, J., & Zettergren, M. (2020). The dynamics of nonlinear atmospheric acoustic-gravity waves generated by tsunamis over realistic bathymetry. *Journal of Geophysical Research: Space Physics*, *125*(12), e2020JA028309. https://doi.org/10.1029/2020JA028309

Jiang, J. H., Eckermann, S. D., Wu, D. L., & Ma, J. (2004). A search for mountain waves in MLS stratospheric limb radiances from the winter Northern Hemisphere: Data analysis and global mountain wave modeling. *Journal of Geophysical Research*, *109*(D3). https://doi.org/10.1029/2003JD003974

Jiang, Q., Doyle, J. D., Eckermann, S. D., & Williams, B. P. (2019). Stratospheric trailing gravity waves from New Zealand. *Journal of the Atmospheric Sciences*, *76*(6), 1565–1586. https://doi.org/10.1175/JAS-D-18-0290.1

Jones, M., Jr., Goncharenko, L. P., McDonald, S. E., Zawdie, K. A., Tate, J., Gasperini, F., et al. (2023). Understanding nighttime ionospheric depletions associated with sudden stratospheric warmings in the American sector. *Journal of Geophysical Research: Space Physics*, *128*(6), e2022JA031236. https://doi.org/10.1029/2022JA031236

Kelley, I. J., Kunduri, B. S. R., Baker, J. B. H., Ruohoniemi, J. M., & Shepherd, S. G. (2023). Storm time electrified MSTIDs observed over mid-latitude north America. *Journal of Geophysical Research: Space Physics*, *128*(3), e2022JA031115. https://doi.org/10.1029/2022JA031115

Klenzing, J., Halford, A. J., Liu, G., Smith, J. M., Zhang, Y., Zawdie, K., et al. (2023). A system science perspective of the drivers of equatorial plasma bubbles. *Frontiers in Astronomy and Space Sciences*, *9*, 1064150. https://doi.org/10.3389/fspas.2022.1064150

Konrad, C. E., & Colucci, S. J. (1989). An examination of extreme cold air outbreaks over eastern North America. *Monthly Weather Review*, *117*(12), 2687–2700. https://doi.org/10.1175/1520-0493(1989)117⟨2687:AEOECA⟩2.0.CO;2

Kretschmer, M., Cohen, J., Matthias, V., Runge, J., & Coumou, D. (2018). The different stratospheric influence on cold-extremes in Eurasia and North America. *npj Climate and Atmospheric Science*, *1*(1), 44. https://doi.org/10.1038/s41612-018-0054-4

Lee, S. H., Furtado, J. C., & Charlton-Perez, A. J. (2019). Wintertime North American weather regimes and the Arctic stratospheric polar vortex. *Geophysical Research Letters*, *46*(24), 14892–14900. https://doi.org/10.1029/2019GL085592

Liu, X., Xu, J., Yue, J., Vadas, S. L., & Becker, E. (2019). Orographic primary and secondary gravity waves in the middle atmosphere from 16-year SABER observations. *Geophysical Research Letters*, *46*(8), 4512–4522. https://doi.org/10.1029/2019GL082256

Lund, T. S., & Fritts, D. C. (2012). Numerical simulation of gravity wave breaking in the lower thermosphere. *Journal of Geophysical Research*, *117*(D21). https://doi.org/10.1029/2012JD017536

Lund, T. S., Fritts, D. C., Wan, K., Laughman, B., & Liu, H.-L. (2020). Numerical simulation of mountain waves over the southern Andes. Part I: Mountain wave and secondary wave character, evolutions, and breaking. *Journal of the Atmospheric Sciences*, *77*(12), 4337–4356. https://doi.org/10.1175/JAS-D-19-0356.1

Lyapustin, A., Alexander, M. J., Ott, L., Molod, A., Holben, B., Susskind, J., & Wang, Y. (2014). Observation of mountain lee waves with MODIS NIR column water vapor. *Geophysical Research Letters*, *41*(2), 710–716. https://doi.org/10.1002/2013GL058770

Makarevich, R. A., & Bristow, W. A. (2014). Fine structure of subauroral electric field and electron content. *Journal of Geophysical Research: Space Physics*, *119*(5), 3789–3802. https://doi.org/10.1002/2014JA019821

Martin, C., Rohel, R., Kunduri, B., Pitzer, P., Khanal, K., Shi, X., et al. (2024). Superdarn/pydarn: Pydarn v4.0 [Software]. *Zenodo*. https://doi.org/10.5281/zenodo.10452339

Martius, O., Polvani, L. M., & Davies, H. C. (2009). Blocking precursors to stratospheric sudden warming events. *Geophysical Research Letters*, *36*(14). https://doi.org/10.1029/2009GL038776

McFarlane, N. (1987). The effect of orographically excited gravity wave drag on the general circulation of the lower stratosphere and troposphere. *Journal of the Atmospheric Sciences*, *44*(14), 1775–1800. https://doi.org/10.1175/1520-0469(1987)044⟨1775:TEOOEG⟩2.0.CO;2

Millin, O. T., Furtado, J. C., & Basara, J. B. (2022). Characteristics, evolution, and formation of cold air outbreaks in the Great Plains of the United States. *Journal of Climate*, *35*(14), 4585–4602. https://doi.org/10.1175/JCLI-D-21-0772.1

Miyoshi, Y., Fujiwara, H., Jin, H., & Shinagawa, H. (2015). Impacts of sudden stratospheric warming on general circulation of the thermosphere. *Journal of Geophysical Research: Space Physics*, *120*(12), 10897–10912. https://doi.org/10.1002/2015JA021894

Niranjan Kumar, K., Ramkumar, T. K., & Krishnaiah, M. (2012). Analysis of large-amplitude stratospheric mountain wave event observed from the AIRS and MLS sounders over the western Himalayan region. *Journal of Geophysical Research*, *117*(D22). https://doi.org/10.1029/2011JD017410

Nishioka, M., Tsugawa, T., Kubota, M., & Ishii, M. (2013). Concentric waves and short-period oscillations observed in the ionosphere after the 2013 Moore EF5 tornado. *Geophysical Research Letters*, *40*(21), 5581–5586. https://doi.org/10.1002/2013GL057963

Nishitani, N., Ruohoniemi, J. M., Lester, M., Baker, J. B. H., Koustov, A. V., Shepherd, S. G., et al. (2019). Review of the accomplishments of mid-latitude Super Dual Auroral Radar Network (SuperDARN) HF radars. *Progress in Earth and Planetary Science*, *6*(1), 27. https://doi.org/10.1186/s40645-019-0270-5

Noll, C. E. (2010). The crustal dynamics data information system: A resource to support scientific analysis using space geodesy. *Advances in Space Research*, *45*(12), 1421–1440. https://doi.org/10.1016/j.asr.2010.01.018

Paziewski, J., Høeg, P., Sieradzki, R., Jin, Y., Jarmolowski, W., Hoque, M. M., et al. (2022). The implications of ionospheric disturbances for precise GNSS positioning in Greenland. *Journal of Space Weather and Space Climate*, *12*, 33. https://doi.org/10.1051/swsc/2022029

Plougonven, R., & Zhang, F. (2014). Internal gravity waves from atmospheric jets and fronts. *Reviews of Geophysics*, *52*(1), 33–76. https://doi.org/10.1002/2012RG000419

Preusse, P., Eckermann, S. D., Ern, M., Oberheide, J., Picard, R. H., Roble, R. G., et al. (2009). Global ray tracing simulations of the SABER gravity wave climatology. *Journal of Geophysical Research*, *114*(D8). https://doi.org/10.1029/2008JD011214

Ralph, F., Neiman, P., & Keller, T. (1999). Deep-tropospheric gravity waves created by leeside cold fronts. *Journal of the Atmospheric Sciences*, *56*(17), 2986–3009. https://doi.org/10.1175/1520-0469(1999)056⟨2986:DTGWCB⟩2.0.CO;2

Regmi, R. P., & Maharjan, S. (2015). Trapped mountain wave excitations over the Kathmandu valley, Nepal. *Asia-Pacific Journal of Atmospheric Sciences*, *51*(4), 303–309. https://doi.org/10.1007/s13143-015-0078-1

Sandu, I., van Niekerk, A., Shepherd, T. G., Vosper, S. B., Zadra, A., Bacmeister, J., et al. (2019). Impacts of orography on large-scale atmospheric circulation. *npj Climate and Atmospheric Science*, *2*(1), 10. https://doi.org/10.1038/s41612-019-0065-9

Sato, K., Tateno, S., Watanabe, S., & Kawatani, Y. (2012). Gravity wave characteristics in the Southern Hemisphere revealed by a high-resolution middle-atmosphere general circulation model. *Journal of the Atmospheric Sciences*, *69*(4), 1378–1396. https://doi.org/10.1175/JAS-D-11-0101.1

Smith, R. B. (2019). 100 years of progress on mountain meteorology research. *Meteorological Monographs*, *59*, 20–21. https://doi.org/10.1175/AMSMONOGRAPHS-D-18-0022.1

Smith, R. B., Skubis, S., Doyle, J. D., Broad, A. S., Kiemle, C., & Volkert, H. (2002). Mountain waves over Mont Blanc: Influence of a stagnant boundary layer. *Journal of the Atmospheric Sciences*, *59*(13), 2073–2092. https://doi.org/10.1175/1520-0469(2002)059⟨2073:MWOMBI⟩2.0.CO;2

Thomas, E. G., & Shepherd, S. G. (2022). Virtual height characteristics of ionospheric and ground scatter observed by mid-latitude superdarn hf radars. *Radio Science*, *57*(6), 1–17. https://doi.org/10.1029/2022rs007429

Timoté, C. C., Juan, J. M., Sanz, J., González-Casado, G., Rovira-García, A., & Escudero, M. (2020). Impact of medium-scale traveling ionospheric disturbances on network real-time kinematic services: CATNET study case. *Journal of Space Weather and Space Climate*, *10*, 29. https://doi.org/10.1051/swsc/2020030

Vadas, S. L., & Becker, E. (2019). Numerical modeling of the generation of tertiary gravity waves in the mesosphere and thermosphere during strong mountain wave events over the southern Andes. *Journal of Geophysical Research: Space Physics*, *124*(9), 7687–7718. https://doi.org/10.1029/2019JA026694

Vadas, S. L., Xu, S., Yue, J., Bossert, K., Becker, E., & Baumgarten, G. (2019). Characteristics of the quiet-time hot spot gravity waves observed by GOCE over the Southern Andes on 5 July 2010. *Journal of Geophysical Research: Space Physics*, *124*(8), 7034–7061. https://doi.org/10.1029/2019JA026693

Wu, D. L., & Zhang, F. (2004). A study of mesoscale gravity waves over the north Atlantic with satellite observations and a mesoscale model. *Journal of Geophysical Research*, *109*(D22). https://doi.org/10.1029/2004JD005090

Zawdie, K., Belehaki, A., Burleigh, M., Chou, M.-Y., Dhadly, M. S., Greer, K., et al. (2022). Impacts of acoustic and gravity waves on the ionosphere. *Frontiers in Astronomy and Space Sciences*, *9*, 1064152. https://doi.org/10.3389/fspas.2022.1064152

Zhang, F., Zhang, M., Wei, J., & Wang, S. (2013). Month-long simulations of gravity waves over North America and North Atlantic in comparison with satellite observations. *Acta Meteorologica Sinica*, *27*(3), 446–454. https://doi.org/10.1007/s13351-013-0301-x

Zhang, J., Xu, J., Wang, W., Wang, G., Ruohoniemi, J. M., Shinbori, A., et al. (2022). Oscillations of the ionosphere caused by the 2022 Tonga volcanic eruption observed with SuperDARN radars. *Geophysical Research Letters*, *49*(20), e2022GL100555. https://doi.org/10.1029/2022GL100555